Oceanologia (2018) 60, 464—477

Available online at www.sciencedirect.com

ScienceDirect

journal homepage: www.journals.elsevier.com/oceanologia/

ORIGINAL RESEARCH ARTICLE

Partitioning of solar radiation in Arctic sea ice during melt season

Peng Lu [a,*], **Bin Cheng** [b], **Matti Leppäranta** [c], **Zhijun Li** [a]

[a] *State Key Laboratory of Coastal and Offshore Engineering, Dalian University of Technology, Dalian, China*
[b] *Finnish Meteorological Institute, Helsinki, Finland*
[c] *Institute of Atmospheric and Earth Sciences, University of Helsinki, Helsinki, Finland*

Received 28 December 2017; accepted 22 March 2018
Available online 10 April 2018

KEYWORDS
Arctic sea ice;
Melt pond;
Radiation transfer;
Mass balance;
Numerical modelling

Summary The partitioning of solar radiation in the Arctic sea ice during the melt season is investigated using a radiative transfer model containing three layers of melt pond, underlying sea ice, and ocean beneath ice. The wavelength distribution of the spectral solar irradiance clearly narrowed with increasing depth into ice, from 350—900 nm at the pond surface to 400—600 nm in the ocean beneath. In contrast, the net spectral irradiance is quite uniform. The absorbed solar energy is sensitive to both pond depth (H_p) and the underlying ice thickness (H_i). The solar energy absorbed by the melt pond (Ψ_p) is proportional only to H_p. However, the solar energy absorbed by the underlying ice (Ψ_i) is more complicated due to the counteracting effects arising from the pond and ice to the energy absorption. In September, Ψ_p decreased by 10% from its August value, which is attributed to more components in the shortwave band (<530 nm) of the incident solar radiation in September relative to August. The absorption coefficient of the sea ice only enhances the absorbed energy in ice, while an increase in the ice scattering coefficient only enhances the absorbed energy in the melt pond, although the resulted changes in Ψ_p and Ψ_i are smaller than that in the albedo and transmittance. The energy absorption rate with depth depends strongly on the incident irradiance and ice scattering, but only weakly on pond depth. Our results are comparable to previous field measurements and numerical simulations. We conclude that the incident solar energy was largely absorbed by the melt pond rather than by the underlying sea ice.

* Corresponding author at: State Key Laboratory of Coastal and Offshore Engineering, Dalian University of Technology, Dalian 116024, China. Tel.: +86 411847085208303; Fax: +86 41184708526.
E-mail addresses: lupeng@dlut.edu.cn (P. Lu), bin.cheng@fmi.fi (B. Cheng), matti.lepparanta@helsinki.fi (M. Leppäranta), lizhijun@dlut.edu.cn (Z. Li).
Peer review under the responsibility of Institute of Oceanology of the Polish Academy of Sciences.

https://doi.org/10.1016/j.oceano.2018.03.002

1. Introduction

A steady decline in Arctic sea ice, especially during the melt seasons since 2000, has been well demonstrated (e.g. Comiso et al., 2017). An increase in solar radiation absorbed by the Arctic Ocean was also observed by satellite instruments during the same period (NASA, 2014). The partitioning of solar radiation in an ice-covered sea is a central issue of the energy budget of the Arctic Ocean and the mass balance of Arctic sea ice (Lei et al., 2016; Wang et al., 2014, 2016). The solar energy absorbed by the sea ice cover largely determines the rate of ice melting (Hudson et al., 2013), while the backscattering part provides heats to the atmosphere (Perovich, 2005). Energy penetrating through the sea ice cover warms up the ocean beneath the ice, which is a primary source of ocean heat (Katlein et al., 2015). The apparent optical properties (AOPs) — albedo (reflectance) and transmittance — determine the partitioning of solar radiation into backscattering, absorption and transmittance in the Arctic sea ice (Perovich, 1996).

Extensive field observations have been carried out to measure the AOPs of first-year (FYI) and multiyear sea ice (MYI), and were employed to parameterize the distribution of solar energy in numerical models (e.g. Taskjelle et al., 2015). In Arctic summer, melt ponds pose notable impacts on the AOPs of sea ice. Not only is the albedo of the melting ice significantly lower than that of dry or snow-covered ice, but melt ponds take more solar radiation which then penetrates the ice (Webster et al., 2015). Even a skim layer of liquid water on an ice surface can change the AOPs considerably (Light et al., 2015). For example, the transmittance through FYI is almost three times larger than through MYI because of the larger melt-pond coverage of FYI, and the energy absorption is also 50% larger in FYI than in MYI (Nicolaus et al., 2012). Ponded ice transmits roughly 4.4 times more total energy into the ocean than nearby bare ice. The ubiquitous surface-scattering layer and drained layer present on bare sea ice are responsible for its relatively high albedo and low transmittance, while light transmittance through ponded ice depends on its physical thickness and the magnitude of the scattering coefficient in the ice interior (Light et al., 2015).

Radiative transfer models (RTM) are another approach to determine the partitioning of solar radiation in melting sea ice. A plane-parallel melt pond model with either a Lambertian or a non-Lambertian reflector for the pond bottom was developed to estimate the pond albedo and radiance distribution in ponded ice (Podgorny and Grenfell, 1996). Solar-radiation flux transfer in melt ponds was simulated by Skyllingstad et al. (2009), and variations in the pond albedo with pond depth and the underlying ice albedo were proposed. Influences of different impact factors on the pond albedo and transmittance were investigated, and a parameterized pond albedo as a function of both pond depth and ice thickness was suggested (Lu et al., 2016). This parameterization is more suitable for thinning Arctic sea ice than the exponential relationship between albedo and pond depth (Morassutti and Ledrew, 1996), which is valid for thicker ice.

A summary of previous field and numerical studies on the AOPs of melting sea ice is listed in Table 1, where α and T denote the percentage of solar energy backscattered by the pond surface and transmitted into the ocean beneath ice, respectively, and Ψ_p and Ψ_i are the fractions absorbed by the melt pond and the underlying ice layer, respectively. Some studies combined the absorption of melt ponds and the underlying ice, and present it as the sum of Ψ_p and Ψ_i.

The results of the studies that considered the partitioning of solar energy in melting sea ice differ widely from each other, as seen in Table 1. One can attribute the variations to the different ice conditions in the studies. As such, a systemic investigation on the various factors that affect the energy distribution is still needed. In addition, the portion of solar energy absorbed by meltwater is obviously larger than that absorbed by underlying sea ice, which argues for the notable capacity of melt ponds in energy absorption, and which also implies the possible complicated processes associated with the allocation of energy to the air, pond, ice, and the water below. However, melt ponds are always treated as a controller of surface albedo, and are not individually considered in numerical models (Pedersen et al., 2009); hence, an investigation of their full physics is required.

To achieve these goals, an RTM initially developed to parameterize melt-pond albedo (Lu et al., 2016) was used. The framework of the RTM is summarized in Section 2. In Section 3 we investigate the distribution of solar radiation, the energy budget in the melting sea ice, and the absorption ratio of solar energy. Discussions on the surface transmission parameter, ice internal melt, and photosynthetically active radiation (PAR) beneath the ice are presented in Section 4. Conclusions are drawn in Section 5.

2. Model description

Radiation transfer in a plane-parallel medium can be simplified as two streams: upwelling and downwelling irradiances. These are governed by two coupled first-order differential equations under the assumptions of diffuse incident solar radiation and isotropic scattering (Flocco et al., 2015):

$$\begin{cases} dF^{\downarrow}(z,\lambda) = -k_\lambda F^{\downarrow}(z,\lambda)dz - \sigma_\lambda F^{\downarrow}(z,\lambda)dz + \sigma_\lambda F^{\uparrow}(z,\lambda)dz \\ dF^{\uparrow}(z,\lambda) = k_\lambda F^{\uparrow}(z,\lambda)dz + \sigma_\lambda F^{\uparrow}(z,\lambda)dz - \sigma_\lambda F^{\downarrow}(z,\lambda)dz \end{cases}, \quad (1)$$

where σ_λ is the wavelength-dependent scattering coefficient and k_λ is the absorption coefficient, which defines the inherent optical properties (IOP) of the medium. $F^{\uparrow}(z, \lambda)$ and $F^{\downarrow}(z, \lambda)$ are the upwelling and downwelling irradiances, respectively, z is the depth in the medium and λ is the wavelength.

The RTM developed by Lu et al. (2016) contains three layers: the melt pond, the underlying ice, and the ocean beneath the ice. Assuming the continuity of radiation flux at each interface between the layers, the irradiance in both directions in the melt pond and underlying ice can be calculated. Two AOPs, the spectral albedo of the melt pond α_λ, and the spectral transmittance T_λ, are determined accordingly.

A two-stream model is employed instead of a more advanced RTM such as the one given by Podgorny et al. (2018) using Monte Carlo approach. This is because the two-stream model is mathematically straightforward, and an analytical solution is available for model validation. Moreover, different studies have revealed that the results of the two-stream RTM using Eq. (1) agree well with field measurements on sea ice (Flocco et al., 2015; Taylor and Feltham, 2004). The drawbacks of such model lie to assumptions of

Table 1 Partitioning of incident solar energy in melting sea ice in Arctic summer, including the fractions reflected back by the ice surface α, absorbed by the melt pond Ψ_p, absorbed by the underlying ice Ψ_i, and transmitted into the ocean beneath ice T. Note that $\alpha + \Psi_p + \Psi_i + T = 100\%$. The sum of Ψ_p and Ψ_i is presented if their individual values were not reported in the references.

References	α [%]	$\Psi_p + \Psi_i$ [%]	T [%]	Ice conditions	
Hudson et al. (2013)	15	46	39	Dark pond on FYI	FM
	34	46	20	Bright pond on FYI	FM
Perovich et al. (2001)	15	73	12	Pond on MYI, August	FM
	35	58	7	Pond on MYI, June	FM
Light et al. (2015)	18	30 + 30	22	Pond on FYI	FM
	25	40 + 25	10	Pond on MYI	FM
Nicolaus et al. (2012)	21	57	22	Pond on FYI	FM
	29	56	15	Pond on MYI	FM
Perovich and Tucker (1997)	24	69	7	Pond on MYI, July	FM
Perovich (2005)	26	57	17	Pond on MYI	FM
Ebert et al. (1995)	20	66 + 12	2	Pond on FYI, July	NS
Podgorny and Grenfell (1996)	13	38 + 38	11	Old pond with LBR	NS
	26	38 + 29	7	Young pond with LBR	NS
	–	38 + 37	–	Old pond with non-LBR	NS
	–	39 + 28	–	Young pond with non-LBR	NS

FM – field measurements. NS – numerical simulation. LBR – Lambertian bottom reflection.

diffuse incident solar radiation in the air and isotropic scattering in the ice. The former assumption is not a major problem in Arctic summer because sky is often covered with low stratus cloud. The latter one is also not badly biased for melting sea ice, because the geometric structure of porous sea ice becomes more irregular that can favour isotropic scattering in the ice (Leppäranta et al., 2003).

The IOPs of sea ice and water are prescribed in this study and follow the previous results in Lu et al. (2016). The wavelength-dependent absorption coefficient of water ($k_{\lambda,w}$) employs the pure water values from Kou et al. (1993) and Smith and Baker (1981). The absorption coefficient of sea ice ($k_{\lambda,i}$) is determined by combining the contributions from pure ice and brine pockets, where absorption in the gas inclusions can be neglected. Scattering in meltwater and the ocean beneath the ice is neglected ($\sigma_{\lambda,w} = 0$) according to previous studies (e.g. Taylor and Feltham, 2004). This has been shown to be a valid approximation for melt ponds with a depth less than 1 m (Podgorny and Grenfell, 1996). And the upwelling radiation backscattered by the ocean beneath ice is also extremely small (~1% of the total upwelling radiative flux) because the scattering coefficient of water is 2–3 orders of magnitude lower than that of sea ice (Smith and Baker, 1981). The scattering coefficient of sea ice is independent of wavelength, and a value of $\sigma_i = 2.5\ m^{-1}$ was promoted for summer Arctic sea ice. The incident solar irradiance $F_0(\lambda)$ measured by Grenfell and Perovich (2008) under a completely overcast sky in August with the solar disc not visible, is employed as a representation of Arctic summer. The considered wavelength range covers the solar spectrum from $\lambda_1 = 300$ nm to $\lambda_2 = 2500$ nm.

3. Results

3.1. Vertical distribution of the spectral irradiance

Different to sea ice, irradiance in the ocean can be expressed by Beer's absorption law if the transmitted irradiance $F_w^{\downarrow}(z_w = 0, \lambda)$ is known, since the ocean may be regarded as a semi-infinite medium with a negligible scattering coefficient:

$$\begin{cases} F_w^{\downarrow}(z_w, \lambda) = F_w^{\downarrow}(0, \lambda)\exp(-k_{\lambda,w} z_w) \\ F_w^{\uparrow}(z_w, \lambda) = 0 \end{cases} \quad (2)$$

The upwelling irradiance beyond the pond surface may also be deduced as $\alpha_\lambda F_0(\lambda)$. Then the distributions of the downwelling and upwelling irradiances in the pond–ice–ocean system are obtained. A typical case with $H_p = 0.3$ m and $H_i = 1.0$ m, corresponding to FYI in Arctic summer season, was implemented to calculate the spectral irradiance distribution. The net irradiance distribution across the ice sheet, $F_{net}(z, \lambda)$, was also calculated, which is the difference between the downwelling and upwelling streams (Fig. 1).

The irradiance in Fig. 1 is continuous in magnitude and spectrum within the three regimes (melt pond, underlying ice and the ocean beneath the ice), and discontinuities occur only at the interface between the air and the pond because of reflections there.

Most of the downwelling incident irradiance in the visible band is dissipated in the pond water and the upper ice layer, and only an irradiance of ~0.1 $W{\cdot}m^{-2}{\cdot}nm^{-1}$ (15% of the maximum in melt pond) at wavelengths 400–600 nm reaches the bottom of the ice (Fig. 1a). The downwelling irradiance in the near-infrared (NIR) band is completely absorbed in the pond water, with none reaching the bottom of the ice. The amount of ultraviolet (UV) radiation is nearly constant in the melt pond, however 80% of its energy is dissipated by the underlying sea ice, leaving only ~0.05 $W{\cdot}m^{-2}{\cdot}nm^{-1}$ in 350–400 nm band transmitting through the sea ice to the ocean below.

The maximum amount of downwelling irradiance exists in the melt pond at a wavelength of 450 nm, 0.6 $W{\cdot}m^{-2}{\cdot}nm^{-1}$, which is even greater than the incident solar radiation. It can be explained by the total reflection of light at the air-pond interface, where the downwelling irradiance, $F_p^{\downarrow}(0, \lambda)$, is the sum of the fraction of the $F_0(\lambda)$ entering the pond and the

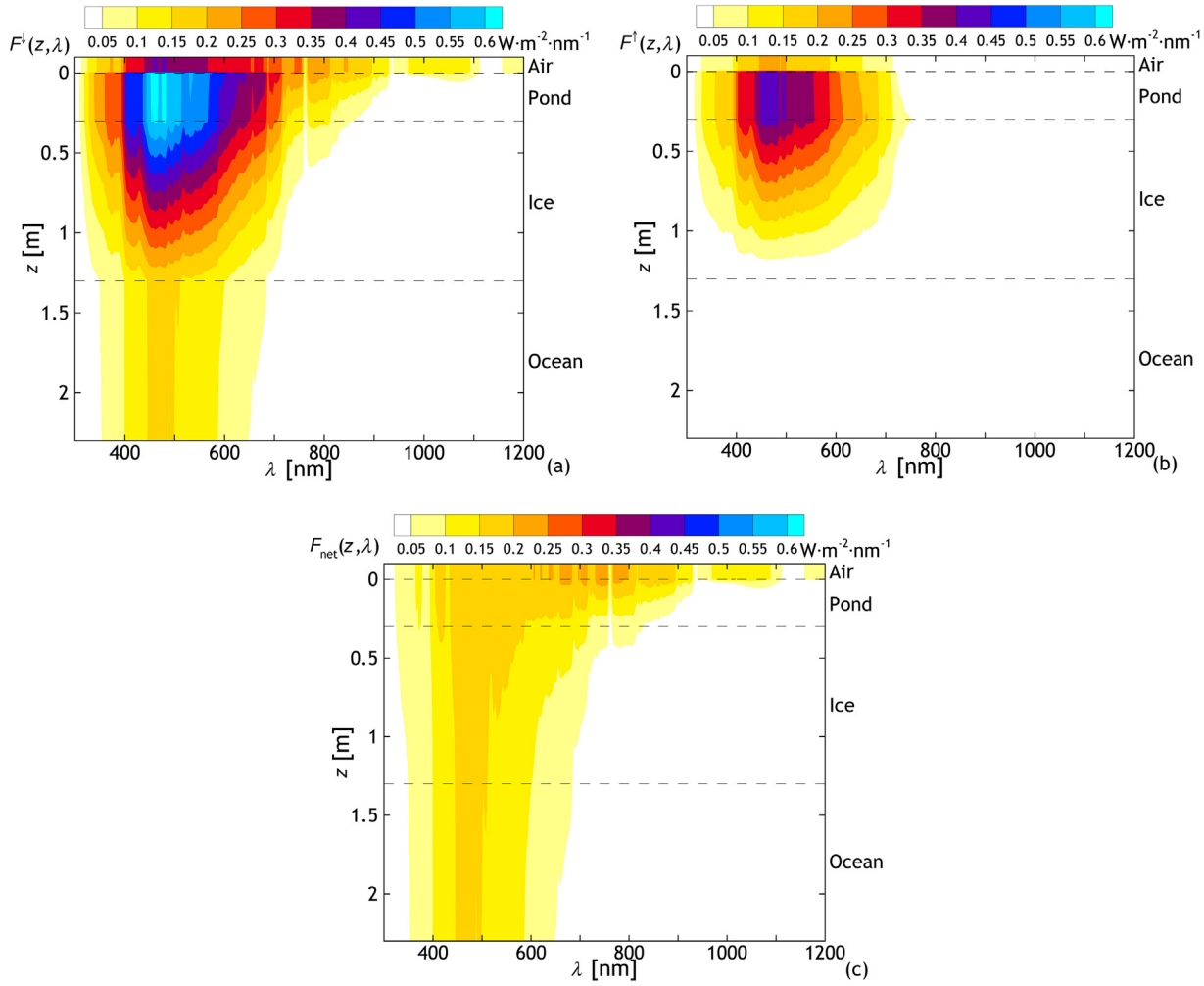

Figure 1 Spectral irradiance distribution in the pond–ice–ocean system with H_p = 0.3 m and H_i = 1.0 m: (a) downwelling irradiance $F^{\downarrow}(z, \lambda)$, (b) upwelling irradiance $F^{\uparrow}(z, \lambda)$, and (c) net irradiance $F_{net}(z, \lambda) = F^{\downarrow}(z, \lambda) - F^{\uparrow}(z, \lambda)$. The colour denotes the spectral value in units of W·m^{-2}·nm^{-1}. Irradiances beyond 1200 nm are truncated in the plots because of their very small quantities. (For interpretation of the references to color in this figure legend, the reader is referred to the web version of this article.)

fraction of the upwelling irradiance reflected downwards by the pond-air interface, $F_p^{\downarrow}(0, \lambda) = (1 - R_1)\, F_0(\lambda) + R_1'\, F_p^{\uparrow}(0, \lambda)$. R_1 = 0.05, which is the Fresnel reflection coefficient at the air-water interface under diffuse sky conditions (Perovich, 1990), and R_1' = 0.54, which is the specular reflectance of the upwelling irradiance at the water-air interface (Dera, 1992). Hence, 95% of the incident solar radiation enters the melt pond, and half of the backscattering irradiance from the underlying ice is reflected back again at the pond surface, where both contribute to a maximum downwelling irradiance that is even greater than $F_0(\lambda)$. On the other hand, the maximum value changes slightly with pond depth because the absorption is very limited ($\sim 10^{-3}$) at 450 nm, and scattering is also negligible in water.

Upwelling irradiance was found only in the pond and ice layers in the visible band (Fig. 1b), because scattering in the ice is the only source of an upwelling stream, and backscattering from water is negligible. Most of the downwelling irradiance into the ice lies in the visible band, so backscattering also occurs in this band. The peak of the upwelling irradiance ($\sim$0.4 W·m^{-2}·nm^{-1} at 450–550 nm) occurs in the upper ice layer and is constant with pond depth owing to the accumulative contributions from the backscatters in the lower ice layer.

The net irradiance is more uniform (0.1–0.2 W·m^{-2}·nm^{-1}) than the downwelling and upwelling irradiances throughout the pond–ice–ocean volume (Fig. 1c). However, the wavelength range clearly narrowed with increasing depth, from 350–900 nm at the pond surface to 400–600 nm in the ocean. The enhanced absorption in ice and water at longer wavelengths is the primary reason for this, which also implies that visible-band radiation is the main contributor to the heat balance in the underlying ice volume and the ocean further below.

3.2. Radiation partitioning in the pond–ice–ocean system

To account for the partitioning of solar energy in the pond–ice–ocean system, the broadband albedo α and transmittance T are defined as:

$$\begin{cases} \alpha = \int_{\lambda_1}^{\lambda_2} \alpha_\lambda F_0(\lambda) d\lambda / Q \\ T = \int_{\lambda_1}^{\lambda_2} T_\lambda F_0(\lambda) d\lambda / Q \\ Q = \int_{\lambda_1}^{\lambda_2} F_0(\lambda) d\lambda \end{cases} \quad (3)$$

We assume that the energy budget in the pond–ice system, and the portion of solar radiation absorbed can be determined by $\Psi = 1 - \alpha - T$. Then, the fraction absorbed by the melt pond Ψ_p, and by the underlying ice Ψ_i, can be individually determined by:

$$\begin{cases} \Psi_p = \int_{\lambda_1}^{\lambda_2} [F_{net}(z_p = 0, \lambda) - F_{net}(z_p = H_p, \lambda)] d\lambda / Q \\ \Psi_i = \int_{\lambda_1}^{\lambda_2} [F_{net}(z_i = 0, \lambda) - F_{net}(z_i = H_i, \lambda)] d\lambda / Q \end{cases} . \quad (4)$$

It is clear that $\Psi = \Psi_p + \Psi_i$. The dependence of the solar energy partitioning in different parts of the melting sea ice with pond depth, H_p, and underlying ice thickness, H_i, is shown in Fig. 2.

The broadband albedo depends mainly on H_i for thin ice ($H_i < 1$ m), but as H_i increases, α is initially sensitive to both H_i and H_p and finally just on H_p for $H_i > 3$ m (Fig. 2a). In contrast, the broadband transmittance depends mostly on H_i, and slightly on H_p (Fig. 2b). This result agrees well with Lu et al. (2016). That is, the portion of solar energy that penetrates all the way to the ocean beneath the ice increases only when the ice becomes thinner, because the extinction effect of ice to the penetrating radiation (absorption + scattering) is stronger than that of water (absorption). However, the portion backscattered by melting ice increases with H_i for thin ice and decreases with H_p for thick ice. This dependence is complicated because a deeper pond poses a negative impact (absorption) on the backscattering, while thicker ice poses both negative (absorption) and positive (scattering) impacts on the backscattering. The overall effect of the ice is positive, however, owing to the larger value of the scattering coefficient relative to the absorption coefficient in the visible band (Fig. 1). The various factors of radiative transfer within the pond and ice cause the backscattering to depend on both H_p and H_i, rather than just one factor, in the whole regime.

The portion of solar energy absorbed by melting sea ice seen in Fig. 2c, increases with both H_i and H_p because either a deeper pond or a thicker underlying ice benefits the absorption of solar radiation. It is interesting if this portion is divided into two. The portion of solar energy absorbed by the melt pond increases only with increasing pond depth (Fig. 2d). The positive effect of backscattering in thicker underlying ice on absorption in melt ponds seems negligible. While the portion absorbed by underlying ice varies in a more complicated way, although the contour lines in Fig. 2e are similar with those seen in Fig. 2a. This can be explained by the counteracting effect of pond and ice to the energy absorption in ice. For a deep pond on thin ice, an increase in ice thickness will significantly enhance the absorbed energy of the underlying ice. For a shallow pond with thick ice, a decrease in pond depth also greatly benefits the absorption by ice. However, for medium values of H_p and H_i, the positive effect of an increase in H_i can be completely counteracted by the negative effect of an increase in H_p. For example, the portion of solar energy absorbed by the underlying ice for H_i = 2 m and H_p = 0.2 m is close to that of the case with H_i = 3 m and H_p = 0.3 m (Fig. 2e).

The relative dominance between the absorbed energy by the pond and ice, namely the ratio of Ψ_p to Ψ_i, is shown in Fig. 2f. It is surprising that the solar energy absorbed by the melt pond is much larger than that by the underlying ice, except for some very shallow ponds with $H_p < 0.1$ m. Indeed, the ratio Ψ_p/Ψ_i even approaches 5–7 for a deep pond on a thin ice layer (Fig. 2f). That is, among the 40–60% solar energy absorbed by melting sea ice (Fig. 2c), a large portion is attributed to the surface water rather than the underlying ice. This again pronounces the importance of melt ponds in enhancing the absorption of sea ice to solar radiation, although part of Ψ_p conducts to the underlying ice.

The solar energy absorbed by melting sea ice ($\Psi_p + \Psi_i$) is dominant with a portion of 40–70%, as seen in Table 1, which agrees with the results in Fig. 2c. Ψ_p/Ψ_i varies within the 1–5.5 range in Table 1, which also approximately agrees with Fig. 2f. The remaining difference can be attributed to the different ice conditions when the field observations were conducted and the definitions used in the numerical modelling. Nevertheless, both results in Table 1 and in Fig. 2 strongly argue for the dominance of solar energy absorption in the melt pond rather than in the underlying ice.

3.3. Impact of other factors on the energy partitioning

Except for the influence of pond depth and the underlying ice thickness, the impacts of other factors to the energy partitioning merit investigation. The values of H_i and H_p are consistent with those in Fig. 1. Variations of the energy partitioning with incident solar irradiance, ice absorption coefficient and ice scattering coefficient are shown in Figs. 3–5, respectively.

Six different incident solar spectra were selected according to Grenfell and Perovich (2008). They were measured near solar noon of the days during the HOTRAX cruise in 2005, and we used them to represent Arctic summer conditions for a completely overcast sky in August and September (Fig. 3a). These six cases differ widely with respect to $F_0(\lambda)$. The broadband albedo and transmittance are slightly higher in September than in August (Fig. 3b). Meanwhile, the portion of solar energy absorbed by the melting sea ice decreases significantly from August to September, in which Ψ_p has a similar trend with Ψ, but Ψ_i is nearly constant in time. This can be attributed to the distribution of the relative energy $F_0(\lambda)/Q$ with wavelength. Although the level of $F_0(\lambda)$ decreases gradually with date (Fig. 3a), more relative energy is contained in the shortwave band (<530 nm) and less in the longwave band (>530 nm). This trend becomes more pronounced with date. As a result, the amount of longwave radiation that can be easily absorbed by surface meltwater decreases significantly with date, and the portion absorbed by the underlying sea ice changes slightly because of the small absorption coefficient of ice in the shortwave band.

Variations in the absorption coefficient of sea ice in Fig. 4a can be attributed to the different combinations of volume fractions of pure ice and brine pockets. However, the difference between the maximum and minimum values of $k_{\lambda,i}$ is

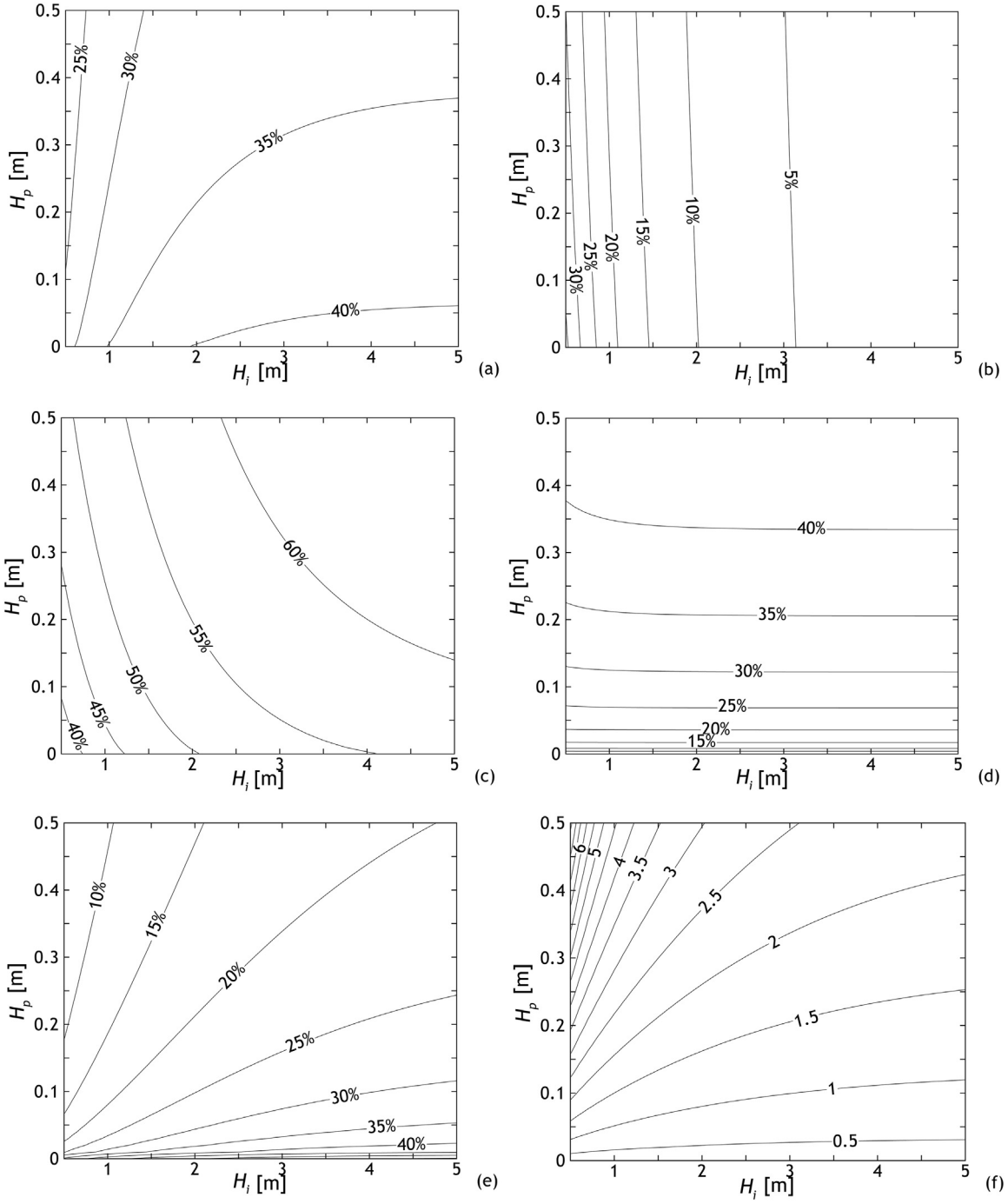

Figure 2 Variations in the portion of solar energy in relation to: (a) the albedo α, (b) transmittance T, (c) the amount absorbed by the melting sea ice Ψ, (d) the amount absorbed by the melt pond Ψ_p, (e) the amount absorbed by the underlying ice Ψ_i, and (f) the ratio of Ψ_p to Ψ_i, with pond depth H_p and the underlying ice thickness H_i. There is $\alpha + T + \Psi = 100\%$, and $\Psi = \Psi_p + \Psi_i$.

still limited, although ν_{pi} and ν_{bp} vary within a relative large range according to the field observations (Huang et al., 2013). As such, variations in the AOPs of the melting sea ice in Fig. 4b are also small. The most obvious change among them is the increase of Ψ_i with increased absorption in the ice. The concurrent slight decrease in Ψ_p is mainly attributed to the enhanced portion of absorption in the ice rather than the decrease in the absolute values of absorption in the melt ponds. Meanwhile, both the broadband albedo and transmittance decrease slightly with increasing absorption in ice, consistent with Lu et al. (2016).

The scattering coefficient of sea ice ranges from 0 to 2.5 m^{-1} in Fig. 5, which corresponds to sea ice from an idealized purely absorbing medium, to melting blue ice with a small content of gas bubbles (1.2 m^{-1}), and then to porous white ice containing large quantities of gas bubbles according to Perovich (1990). Compared with the obvious changes in the broadband albedo and transmittance, variations in the

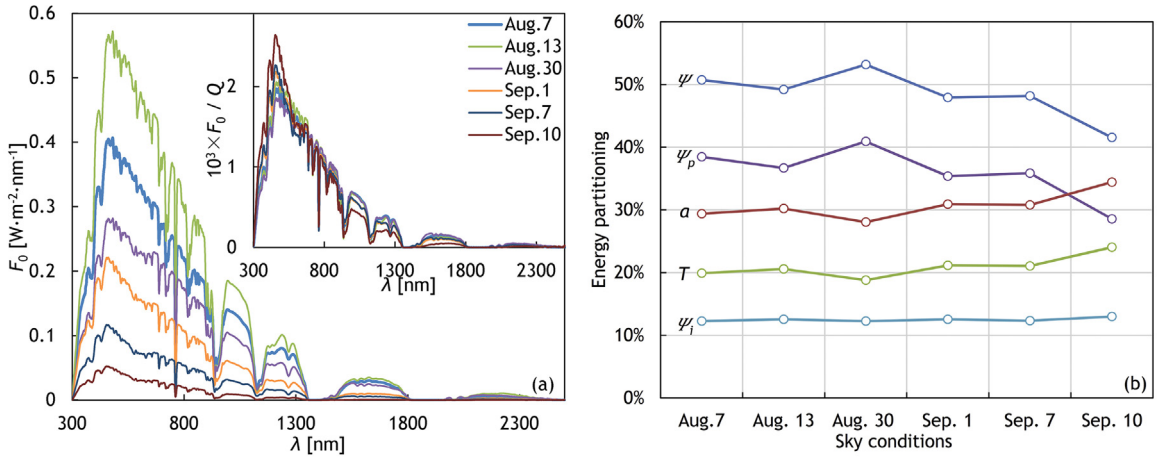

Figure 3 (a) Typical spectral incident solar irradiance in the Arctic summer for a completely overcast sky, according to Grenfell and Perovich (2008). The subplot denotes the normalized values of spectral incident irradiance, which are equal to the ratio of F_0 to the wavelength-integrated incident irradiance Q. (b) The influence on the portion of solar energy in the melting sea ice for H_p = 0.3 m and H_i = 1.0 m. Recall $\alpha + T + \Psi = 1$, and $\Psi = \Psi_p + \Psi_i$. The spectral irradiance on August 7 in (a) is the default value of F_0 defined previously.

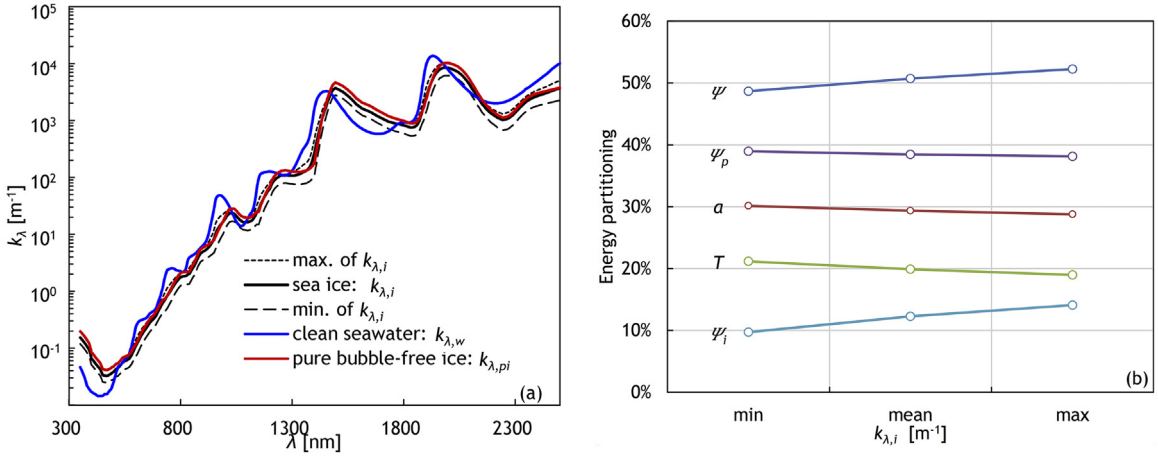

Figure 4 (a) Absorption coefficients of clean seawater, pure bubble-free ice and sea ice. The value of $k_{\lambda,i}$ value is calculated as $k_{\lambda,i} = \nu_{pi}k_{\lambda,pi} + \nu_{bp}k_{\lambda,w}$, which is based on volume fractions of $\nu_{pi} \geq 60\%$ and $\nu_{bp} \leq 20\%$, as determined from field observations of summer Arctic sea ice (Huang et al., 2013). (b) The influence of the ice absorption coefficient on the portion of solar energy in the melting sea ice for H_p = 0.3 m and H_i = 1.0 m.

portion of solar energy absorbed by the melting sea ice are relative small. The portion of absorption in ice is nearly constant in Fig. 5 because the increasing ice-scattering coefficient only causes more upwelling irradiance through backscattering. However, the portion of absorption in the surface meltwater increases consequently owing to the enhanced backscattering irradiance that is absorbed again by the meltwater. Both contribute to the small increase in the portion of solar energy absorbed by melting sea ice.

3.4. Energy absorption rate

The rate of energy absorbed per unit volume (ω) is noteworthy because it is an important source term in the equation of heat conduction, which describes the contribution of solar radiative heating to warming and melting in sea ice. The energy absorption rate ω is given by (Taylor and Feltham, 2004):

$$\omega = -\int_{\lambda_1}^{\lambda_2} \frac{\partial F_{net}(z,\lambda)}{\partial z} d\lambda. \quad (5)$$

Variations in ω vertically downwards in the pond–ice–ocean system for different values of the incident solar radiation, pond depth and underlying ice thickness, and IOPs of the sea ice, are shown in Fig. 6.

Generally, the rate of energy absorption is greatest at the pond surface, which then drops off rapidly by an order of magnitude in the first 0.3 m owing to the loss of radiation in the NIR band, and then decreases more gradually with the attenuation of the remaining radiation. Sudden changes in ω seen at the pond–ice and ice–ocean interfaces in Fig. 6 are mainly attributed to the different IOPs of the two media.

Scattering in ice weakens the energy absorption rate of ice, although the energy fluxes are continuous at the interfaces.

Variations in sky conditions do not alter the relative magnitude of the energy absorption curves to any extent (Fig. 6a), but the absolute values of ω are strictly sorted according to the sequence of the incident energy (Fig. 3a).

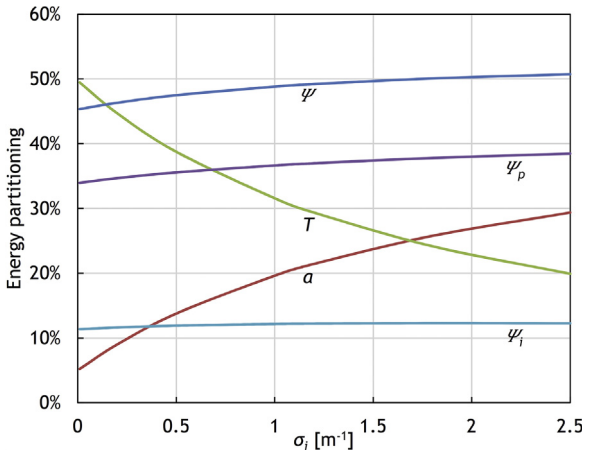

Figure 5 The influence of the ice scattering coefficient on the portion of solar energy in the melting sea ice for H_p = 0.3 m and H_i = 1.0 m.

Near the pond surface, the absorption in August 7 is about 15 times greater than in September 10. This decreases gradually to 10 at a depth of about 0.7 m, and then remains at a relatively constant level, which approximates the ratio of the integrated irradiance for these two sky conditions, namely 10.3 in Fig. 3a.

The influence of scattering in ice is more interesting (Fig. 6b). The energy absorption in the pond water and upper ice layer is greatest for ice with the largest quantity of gas bubbles—that is, the highest scattering coefficient—but it falls below the value for ice with fewer bubbles at a depth of about 0.9 m. This is because the higher scattering in ice results in greater extinction in the upper layer of the pond–ice system and lower transmission to the interior of the ice, whereas more radiation penetrates deep into ice with fewer bubbles, adding to the energy input to the interior of the ice.

Increasing pond depth reduces the energy absorption at the pond's bottom (Fig. 6c) because more radiation is dissipated in the pond water. However, the ice layer acts as a filter, so that the energy absorption at the bottom of the ice, and the consequent transfer of energy into the underlying ocean, is almost uniform. An increase in the ice thickness (Fig. 6d) does not alter the energy absorption by the pond water, but it significantly reduces the absorption at the bottom of the ice and the transfer into the underlying ocean.

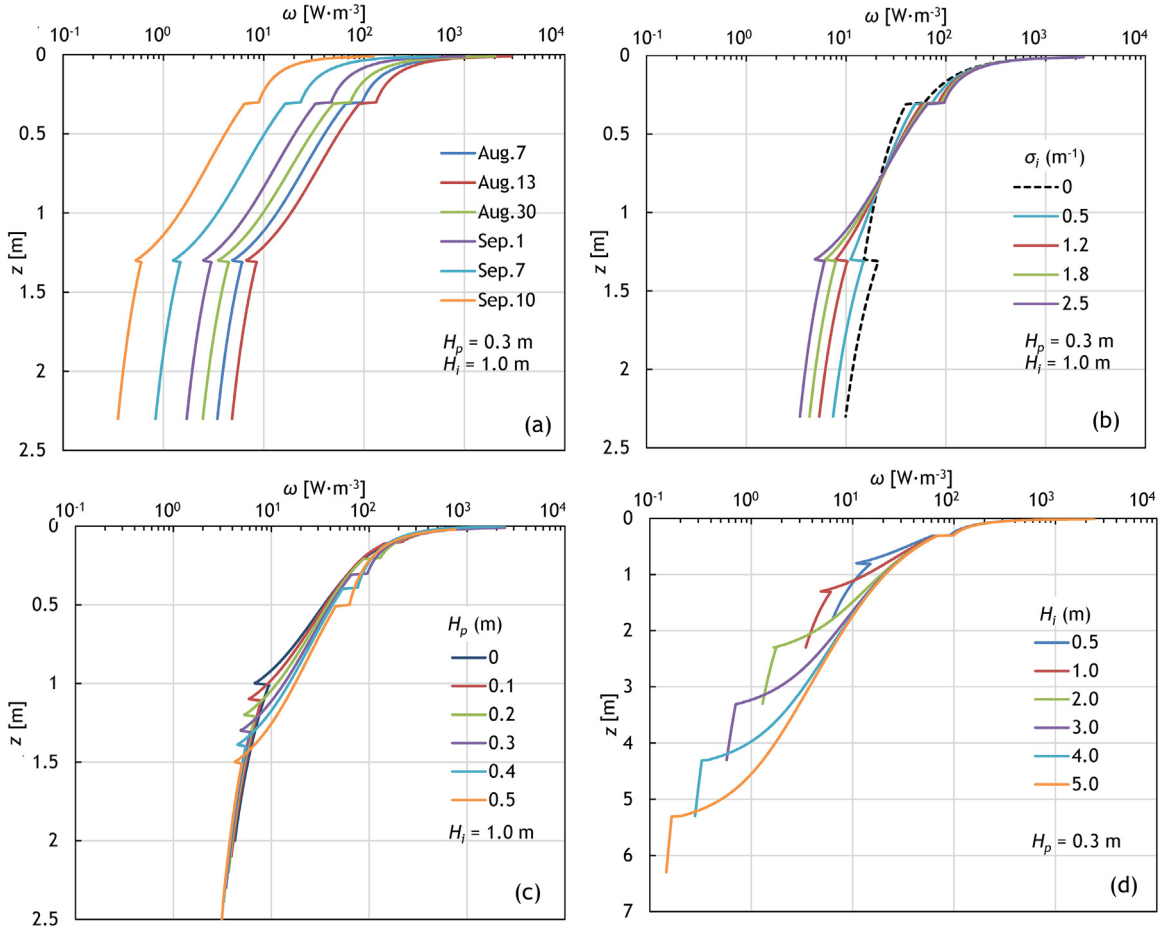

Figure 6 Variations in the rate of absorbed energy ω in the pond–ice–ocean system vertically downwards for different: (a) incident solar irradiance, (b) ice scattering coefficient, (c) pond depth, and (d) underlying ice thickness.

At the same depth, however, due to scattering by the ice, the energy absorption rate within the ice volume is higher when the underlying ice is thicker.

4. Discussion

4.1. The surface transmission parameter I_0

I_0 was designed to quantitatively measure the fraction of radiation transmitted through the highly scattering surface of the ice (Hoffman et al., 2014; Light et al., 2008), and it permits the calculation of shortwave solar radiation within the ice in global climate models (GCMs). The equation for I_0 is given by:

$$I_0 = \frac{\int_{\lambda_1}^{\lambda_2} F_{net}(z = 0.1\,\mathrm{m}, \lambda) d\lambda}{\int_{\lambda_1}^{\lambda_2} F_{net}(z = 0, \lambda) d\lambda}, \quad (6)$$

where $F_{\mathrm{net}}(\lambda,\ z = 0.1\ \mathrm{m})$ is the spectral net flux at 0.1 m depth, and $F_{\mathrm{net}}(\lambda,\ z = 0)$ is the spectral net flux at the surface, which is equal to $F_0(1 - \alpha_\lambda)$. The surface layer thickness is 0.1 m, which was first defined by Maykut and Untersteiner (1971) to conform to their grid spacing and then inherited in following studies.

In most GCMs, I_0 is a constant. For example, values of 0.7 and 0 for I_0 in the visible and NIR bands, respectively, were suggested in CCSM3 (Briegleb et al., 2004). However, I_0 should be variable for ponded sea ice according to Eq. (6). Both H_i and H_p pose an impact on the values of the spectral net flux, and then on the value of I_0. The results are shown in Fig. 7, where the values of I_0 for the visible band were determined with Eq. (6) using $\lambda_1 = 400$ nm to $\lambda_2 = 700$ nm, while $\lambda_1 = 300$ nm to $\lambda_2 = 400$ nm for the UV band, and $\lambda_1 = 700$ nm to $\lambda_2 = 2500$ nm for the NIR band.

Variations of I_0 in the given ranges of H_i (0.5–5 m) and H_p (0–0.5 m) are limited, with broadband values of 0.59 ± 0.03, 0.97 ± 0.01 for the UV band, 0.94 ± 0.01 for the visible band and 0.36 ± 0.02 for the NIR band, respectively (Fig. 7). These are different to the recommendations in CCSM3 (Briegleb et al., 2004), but close to the results of Light et al. (2008), where $I_0 = 0.99$ and 0.48 for ponded MYI in the UV and visible band and NIR band, respectively.

For shallow ponds with depths < 0.1 m, the surface transmission parameter I_0 decreases significantly with increasing H_i for thin ice ($H_i < 2$ m) but with increasing H_p for thick ice

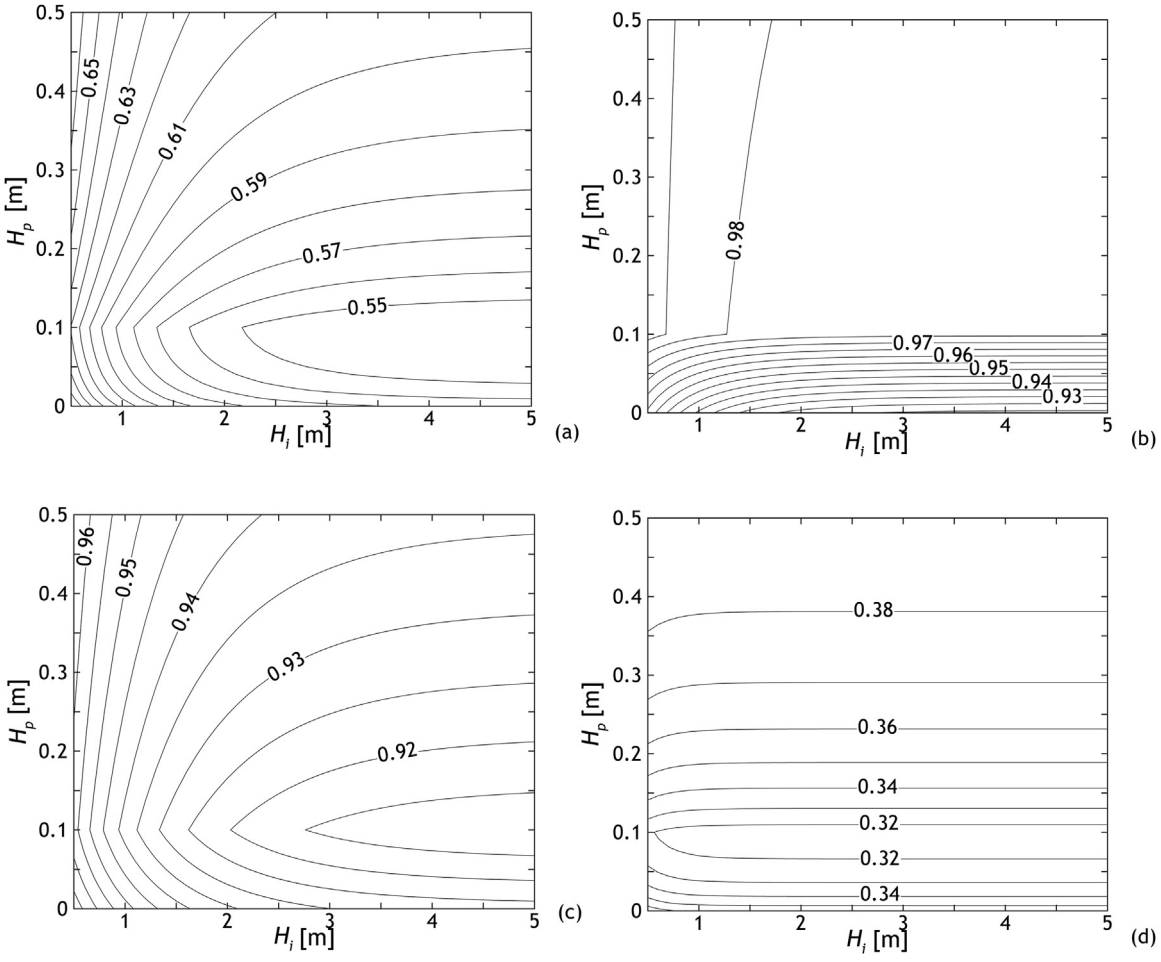

Figure 7 Variations of the surface transmission parameter I_0 with pond depth, H_p, and underlying ice thickness, H_i. In (a) we can see the broadband value of I_0, while in (b), (c), and (d) the results for the UV band (300–400 nm), visible band (400–700 nm), and NIR band (700–2500 nm) are respectively shown. Note that the 0.1-m-thick surface layer contains surface meltwater and upper underlying ice for $H_p < 0.1$ m, and only upper meltwater layer as $H_p \geq 0.1$ m.

($H_i > 3$ m) (Fig. 7a). For ponds deeper than 0.1 m, the behaviour of I_0 is different: it still decreases with increasing H_i for thin ice, but increases with increasing H_p for thick ice. That means that the impact of H_p on I_0 is opposite for shallow and deep ponds. Such a trend is also argued by Fig. 7c and significantly in Fig. 7d, where the value of I_0 in the NIR band depends almost on H_p. However, variations in the UV band are different (Fig. 7b): I_0 in the UV band is almost constant (0.98) as $H_p > 0.1$ m, but it increases with pond depth as $H_p < 0.1$ m, opposite to that in Fig. 7a. A weak dependence on H_i can be only detected for thin ice ($H_i < 1$ m) in Fig. 7b.

It is easy to understand the impact of H_i on I_0, because a thicker ice layer introduces more backscattering, thus weakening transmission through the surface layer. However, for very thick ice, most of the incident radiation in the NIR band is absorbed in the first few centimetres into the meltwater or ice because of the large absorption in this band (Fig. 4a), so that any further increase in H_i will not further alter the value of I_0 (Fig. 7d). Similarly, backscattering in the UV band is very small because less incident radiation in the UV band can penetrate into deeper ice (Fig. 1c), i.e. for a UV absorption coefficient of $\sim 10^{-1}$ m^{-1}, therefore the value of I_0 in the UV band does not depend on H_i for thick ice (Fig. 7b).

The impact of H_p on I_0 is more complicated. For a deep pond ($H_p > 0.1$ m), a further increase in H_p will reduce the amount of incident radiation reaching the underlying ice, which results in less backscattering into the melt pond. Transmission through the 10-cm meltwater layer increases as a result. In contrast, an increase in H_p for a shallow pond ($H_p < 0.1$ m) will significantly enhance the absorption in meltwater because of the large absorption coefficient in the NIR band (Fig. 4a), therefore less incident radiation will reach the lower boundary of the 10-cm surface layer. This also explains why the impact of H_p on I_0 is enhanced in the NIR band (Fig. 7d). However, there is little difference in the UV band. The incident radiation is nearly constant in the melt pond (Fig. 1a) because of the small absorption coefficient of water in the UV band (Fig. 4a), and any increase in H_p will not change the situation very much. So, I_0 in the UV band is constant as $H_p > 0.1$ m. For $H_p < 0.1$ m, a larger H_p causes a smaller H_i within the 10-cm-thick surface layer, and less backscattering due to ice, and finally more transmission through the surface layer (Fig. 7b).

4.2. The internal melting of ponded ice

Internal melting is an important process of sea ice in the melting season (Huang et al., 2016). Different to the surface and basal melting which changes the ice thickness directly, internal melting changes the internal inclusions in sea ice, and ice crystals transform into liquid water pockets (Leppäranta, 2015) that further affect the mechanical and thermal properties of the sea ice (Light et al., 2003). To properly account for internal melting necessitates the inclusion of ice porosity as a dependent model variable. Leppäranta (2009) considered a two-phase approach with liquid phase and solid phase portions considered in each grid cell in addition to the temperature.

The same approach can be employed when considering the internal melting of the sea ice below a melt pond. For simplicity, the temperature profile is taken as isothermal in the underlying ice, which is equal to the freezing point, and the salinity profile is also uniform in depth. These assumptions are acceptable for melting sea ice according to field observations (Polashenski et al., 2012). Then, the amount of absorbed solar energy by the underlying ice will increase the porosity only, and the heat fluxes from the melt pond and the ocean beneath the ice will alter the pond–ice and ice–ocean interfaces, respectively. Consequently, the model physics can be presented as:

$$\begin{aligned} &\text{Surface}: Q_p = -\rho_i L \frac{dH_i^s}{dt}, \\ &\text{Internal}: \quad \omega = \rho_i L \frac{d\nu}{dt}, \\ &\text{Bottom}: \quad Q_w = -\rho_i L \frac{dH_i^b}{dt}, \end{aligned} \tag{7}$$

where Q_p and Q_w are the heat fluxes from the melt pond and the ocean beneath the ice, respectively, ρ_i is the ice density, L is the latent heat of fusion, ν is the liquid water content (essentially the porosity of ice), and ω is the energy absorption rate defined in Eq. (5). Superscripts s and b denote the change of ice thickness H_i occurring on ice surface and bottom, respectively.

For the initial condition of $H_p = 0.3$ m and $H_i = 1.0$ m, evolutions of the ice porosity and thickness can be estimated according to Eq. (7). At each time step, the solar energy absorbed by the melt pond and the ocean beneath the ice for a constant F_0 (same with that in Fig. 2) can be determined by Eq. (7). Half of the solar energy absorbed by the melt pond, $\Psi_p Q$, is assumed to conduct to sea ice according to Zhang et al. (2014), and 5% of the transmitted energy, TQ, contribute to basal melt, which approximately agrees with the oceanic heat flux of 2 W m^{-2} in most GCMs. That is, $Q_p = 0.5\ \Psi_p Q$ and $Q_w = 0.05\ TQ$. Surface melting of the underlying ice contributes only to an increase of pond depth, and the drainage of meltwater into the ocean is neglected as in Lu et al. (2016). That is, $\Delta H_p = \Delta H_i^s \cdot \rho_i / \rho_w$, where ρ_w is the water density. Our result is shown in Fig. 8.

During the modelled one-month melt season, the underlying ice thickness decreased from 1 m to 0.46 m, which includes a surface melt of 0.44 m and a basal melt of 0.02 m (Fig. 8). Consequently, the ice porosity increased from idealized zero with depth, to 0.29 at the surface and 0.06 at the bottom. It is noticeable that once the porosity of the ice reaches 0.3–0.5, the ice can no longer bear its own weight, and subsequently breaks into smaller pieces into the water (Leppäranta, 2009). Hence, in the real initial case with $\nu > 0$, sea ice tends to break up before the thickness decreases to half of its initial value during the melting process. Structural defects will appear first in the upper layer of ice because of the larger ice porosity there, as according to Fig. 8. Additionally, the oceanic heat flux used for the basal melt of sea ice comes only from the transmitted solar radiation in Eq. (7). However, an upwelling heat stream seasonally of up to 10 W m^{-2} due to mixing with warmer underlying water has been also observed in the Arctic Ocean (Polyakov et al., 2017). If the extra heat flux is added to Q_w, the basal melt rate in Fig. 8 will increase by roughly 3 mm day^{-1}, resulting in 0.1 m more basal melt in the one-month melt season. However, the extra heat flux from deep ocean has only a minor impact on the surface melt and

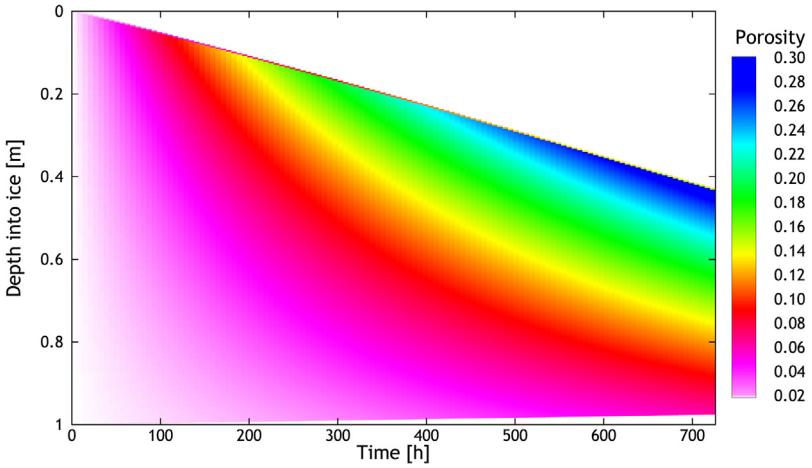

Figure 8 Evolutions of the porosity and thickness of the underlying ice in the model defined by Eq. (7). The *y*-axis denotes the vertical position relative to the initial ice thickness, whereby the changes in ice thickness due to surface melt and basal melt with time can be presented.

porosity evolution of sea ice, because Ψ_p is only sensitive to H_p and the extra decrease in H_i affects T more significantly than Ψ_i (Fig. 2).

The results in Fig. 8 also argue for the importance of including ice porosity in numerical models in addition to temperature and salinity. First, ice porosity describes the phase changes between ice crystal and liquid water, which agree more with actual physical conditions that occur in interior ice during melting and freezing (Light et al., 2003). This is particularly important for melting ice in the summer, because when the ice temperature is close to the freezing point, any additional heat flux will introduce phase changes that alter the ice porosity. Secondly, ice porosity has an upper limit, as mentioned earlier, so modelled ice thickness actually cannot decrease to zero as ice has already broken into pieces due to its weight. Finally, some thermal properties, such as the latent heat of fusion and the specific heat capacity, are also sensitive to the phase components in the sea ice (Shokr and Sinha, 2015). They are constants in most models, but they can be treated as variables that contribute to the ice mass balance if ice porosity changes during the melt process in future.

4.3. The PAR beneath ice

The solar radiation transmitted to the ocean beneath the sea ice impacts not only the physical properties of the system, but also biological processes and biogeochemical fluxes in the sea ice and the uppermost ocean (Arndt et al., 2017). However, only the solar radiation in the visible band can be employed by photosynthetic organisms to the process of photosynthesis. This spectral region corresponds to the range of light visible to the human eye, which is also consistent with the wavelength range in Fig. 1c that most of the transmitted radiation lies in. There are two different ways to quantify PAR: the power of the irradiance, from the point of view of energy transfer, and quantum irradiance q, from the point of view of the flow of light quanta. The total scalar irradiance $E_0(z, \lambda)$, usually employed in biological studies and defined as the irradiance on a point from all directions weighted equally, can be estimated from the planar irradiance $F(z, \lambda)$ employed in Eq. (1):

$$E_0(z,\lambda) = a_u F^{\uparrow}(z,\lambda) + a_d F^{\downarrow}(z,\lambda), \tag{8}$$

where $1 \le a_u,\ a_d \le 2$, and for diffuse radiation, the coefficients are 2. Then, in the ocean beneath ice, there are:

$$\begin{cases} E_0(z_w,\lambda) = 2F_w^{\downarrow}(z_w,\lambda) \\ \hat{E}(z_w) = \int_{\lambda_1}^{\lambda_2} E_0(z_w,\lambda)\,d\lambda \quad q(z_w) = \int_{\lambda_1}^{\lambda_2} E_0(z_w,\lambda)\frac{\lambda}{hc_0}d\lambda, \end{cases} \tag{9}$$

where $h = 6.2566 \times 10^{-34}$ J s is the Planck constant, and $c_0 = 2.9979 \times 10^8$ m s^{-1} is the velocity of light in a vacuum. $\lambda_1 = 400$ nm and $\lambda_2 = 700$ nm are employed in the calculation of PAR.

The ratio $q/\hat{E}$ changes with variations in the spectral distribution of the irradiance rather than its level (Leppäranta et al., 2003; Reinart et al., 1998). So, it is interesting to see how the ratio changes with the properties of the melt pond and the underlying ice. Our results are shown in Fig. 9.

The quantum irradiance q of the PAR transmission drops from 460 μmol·m^{-2}·s^{-1} to 30 μmol·m^{-2}·s^{-1} as H_i increases from 1.3 m to 5.0 m, and the influence of H_p is limited (Fig. 9a). The weakening transmission due to increasing ice thickness is the direct reason for this, and therefore the variations in q are similar with those seen for the transmittance (Fig. 2b). A threshold level of q for primary production is around 10 μmol·m^{-2}·s^{-1}; therefore the PAR transmission for melting Arctic sea ice can of course satisfy this standard.

Within the given range of H_p and H_i, $q/\hat{E}$ = 4.27 ± 0.10 μmol·J^{-1}. The dependence of $q/\hat{E}$ on H_i is obviously greater than on H_p. With increasing ice thickness, the transmitted PAR into the ocean beneath the ice decreases accordingly, and the ratio $q/\hat{E}$ also decreases. In air it is normally assumed that the spectrum of sunlight PAR is even, thus $q/\hat{E}$ = 4.60 μmol·J^{-1}. Here we have a lower value, which means longer wavelengths rather than short ones penetrate the ice. This is an important parameter as such.

Vertical distributions of the ratio $q/\hat{E}$ with depth for different combinations of H_i and H_p are shown in Fig. 9b.

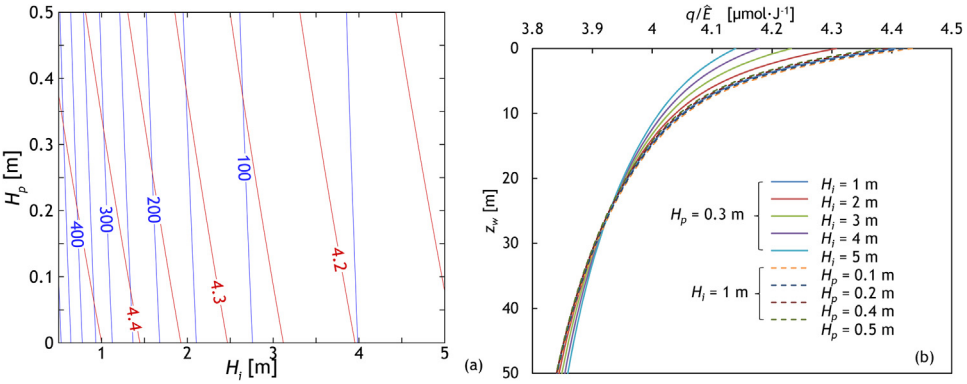

Figure 9 (a) Variations of the quantum irradiance q (blue lines), and the ratio $q/\hat{E}$ (red lines) at the bottom of the ice for a pond depth of H_p and an underlying ice thickness of H_i. (b) Vertical profiles of the ratio $q/\hat{E}$ in the ocean beneath ice. The units of q are μmol·m^{-2}·s^{-1} and μmol·J^{-1} for $q/\hat{E}$. (For interpretation of the references to color in this figure legend, the reader is referred to the web version of this article.)

It is found that a thicker ice layer gives a smaller $q/\hat{E}$ value at the ice bottom, but the value drops slower with depth as compared with that of a thinner ice layer. Thus, at a depth of 25 m beneath the ice, $q/\hat{E}$ = 3.93 for all cases. Below this depth, the $q/\hat{E}$ value for thicker ice is gradually beyond that for thinner ice. The influence of H_p on the profile of $q/\hat{E}$ can be neglected.

5. Conclusions

A two-stream RTM was employed to study the partitioning of solar radiation in the Arctic sea ice during the melt season. Variations of the incident irradiance with depth into the melting sea ice were obtained. Portions of the backscattered solar energy, the fraction absorbed by the melt pond and the underlying ice, and that which penetrates into the ocean beneath the ice were investigated together with their variations due to difference impact factors. Changes in the energy absorption rate were also determined, which were shown to be a contribution of solar radiative heating to thermodynamic equilibrium of sea ice.

The spectral downwelling irradiance distribution clearly narrowed in wavelength, and decreased in value, with increasing depth into the pond–ice–ocean system. Upwelling irradiance resulting from backscattering in ice occurred only in the visible band. The net irradiance was quite uniform, but its wavelength range also narrowed with increasing depth, from 350–900 nm at the pond surface to 400–600 nm in the ocean water. The solar radiation that contributed to the heat balance in the underlying ice volume and the ocean beneath the ice occurred only in the visible band.

Both pond depth, H_p, and the underlying ice thickness, H_i, pose an important impact on the partitioning of solar radiation. The transmitted solar energy into the ocean is sensitive only to H_i, while the backscattered solar energy depends more on H_i than on H_p for thin ice, consistent with the previous results in Lu et al. (2016). The portion absorbed by melting sea ice increased with both H_i and H_p. Among them, the portion in melt pond increased only with H_p, and the variations in the portion in the underlying ice were seen to be complex because of the counteracting effects of pond and ice to the energy absorption in ice. Moreover, the solar energy absorbed by the melt pond was several times larger than that by the underlying ice except for some very shallow ponds ($H_p < 0.1$ m).

The influence of the level of the incident solar irradiance was limited, but the portion of solar energy absorbed by the melt pond decreased by 10% from August to September, which is attributed to the more energy contained in the shortwave band (<530 nm) relative to the longwave band (>530 nm) in September than in August. The portion of solar energy absorbed by the underlying ice increased by 5% as the ice-absorption coefficient increased. As the ice-scattering coefficient increased, the portion of absorption in the ice was nearly constant, but the portion of absorption in the melt pond consequently increased by 5%, in contrast to the obvious changes in the albedo (25%) and transmittance (30%).

Variations in the profile of the energy absorption rate in the melting sea ice showed a strong dependence on the incident irradiance and scattering in ice, but only a weak dependence on pond depth. The increasing ice thickness only reduced the absorption rate in the ocean beneath the ice. Discussions on the surface transmission parameter showed that I_0 decreased with an increase in H_i, but the effect of H_p on I_0 was opposite for shallow and deep ponds. Moreover, variations of I_0 in the UV band were different to those in the visible and NIR bands. Increasing the ice thickness reduced both the quantum irradiance and the ratio $q/\hat{E}$ for the PAR transmission, and also slowed down the attenuation rate of $q/\hat{E}$ in the ocean. The impact of H_p on the PAR beneath ice was limited. Our idealized modelling of the evolution of ice porosity argues for the importance of including ice porosity in numerical models especially for melting sea ice in summer.

Our results agree well with previous field measurements and numerical simulations. More importantly, we demonstrated that the amount of solar energy absorbed by the melt ponds is much larger than that by the underlying ice. Contrary to bare ice, which reflects most of the incident solar radiation, a thin layer of meltwater not only makes the underlying ice absorb more solar energy, but it also creates a situation where the ice is surrounded by two warm water

layers. The upper layer is the melt pond absorbing most solar radiation, and the lower is the ocean mixed layer absorbing nearly 10% more transmitted radiation. Both enhance the melting of sea ice. However, we still have little knowledge on the assignment of absorbed solar energy by melt ponds. Further investigations on how this large part of solar energy is assigned to warm the underlying ice, diffuse to the upper atmosphere, and warm the pond water are still need.

Acknowledgements

This research was supported by the Global Change Research Programme of China (2015CB953901), the National Natural Science Foundation of China (41676187 and 41376186). B.C. was supported by the NSFC research facility mobility (41428603) and the Academy of Finland (283101). M.L. was supported by the EU FP7 Project EuRuCAS (European-Russian Centre for Cooperation in the Arctic and Sub-Arctic Environmental and Climate Research, Grant no. 295068) and the Academy of Finland (11409391).

References

Arndt, S., Meiners, K.M., Ricker, R., Krumpen, T., Katlein, C., Nicolaus, M., 2017. Influence of snow depth and surface flooding on light transmission through Antarctic pack ice. J. Geophys. Res. Oceans 122 (3), 2108—2119, http://dx.doi.org/10.1002/2016JC012325.

Briegleb, B.P., Bitz, C.M., Hunke, E.C., Lipscomb, W.H., Holland, M. M., Schramm, J.L., Moritz, R.E., 2004. Scientific Description of the Sea Ice Component in the Community Climate System Model, version 3. Natl. Cent. for Atmos. Res., Boulder, Colo., NCAR/TN-463+STR, 70 pp.

Comiso, J.C., Meier, W.N., Gersten, R., 2017. Variability and trends in the Arctic Sea ice cover: results from different techniques. J. Geophys. Res. Oceans 122 (8), 6883—6900, http://dx.doi.org/10.1002/2017JC012768.

Dera, J., 1992. Marine physics. Elsevier Oceanogr. Ser. 53, Amsterdam-Oxford-New York-Tokyo-Warsaw, 510 pp.

Ebert, E.E., Schramm, J.L., Curry, J.A., 1995. Disposition of solar radiation in sea ice and the upper ocean. J. Geophys. Res. 100 (C8), 15965—15975, http://dx.doi.org/10.1029/95JC01672.

Flocco, D., Feltham, D.L., Bailey, E., Schroeder, D., 2015. The refreezing of melt ponds on Arctic sea ice. J. Geophys. Res. Oceans 120 (2), 647—659, http://dx.doi.org/10.1002/2014JC010140.

Grenfell, T.C., Perovich, D.K., 2008. Incident spectral irradiance in the Arctic Basin during the summer and fall. J. Geophys. Res. 113 (D12), 13 pp., http://dx.doi.org/10.1029/2007JD009418.

Hoffman, M.J., Fountain, A.G., Liston, G.E., 2014. Near-surface internal melting: a substantial mass loss on Antarctic Dry Valley glaciers. J. Glaciol. 60 (220), 361—374, http://dx.doi.org/10.3189/2014JoG13J095.

Huang, W., Lei, R., Ilkka, M., Li, Q., Wang, Y., Li, Z., 2013. The physical structures of snow and sea ice in the Arctic section of 150°—180°W during the summer of 2010. Acta Oceanol. Sin. 32 (5), 57—67, http://dx.doi.org/10.1007/s13131-013-0314-4.

Huang, W., Lei, R., Han, H., Li, Z., 2016. Physical structures and interior melt of the central Arctic sea ice/snow in summer 2012. Cold Reg. Sci. Technol. 124 (1), 127—137, http://dx.doi.org/10.1016/j.coldregions.2016.01.005.

Hudson, S.R., Granskog, M.A., Sundfjord, A., Randelhoff, A., Renner, A.H.H., Divine, D.V., 2013. Energy budget of first-year Arctic sea ice in advanced stages of melt. Geophys. Res. Lett. 40 (11), 2679—2683, http://dx.doi.org/10.1002/grl.50517.

Katlein, C., Arndt, S., Nicolaus, M., Perovich, D.K., Jakuba, M.V., Suman, S., Elliott, S., Whitcomb, L.L., McFarland, C.J., Gerdes, R., Boetius, A., German, C.R., 2015. Influence of ice thickness and surface properties on light transmission through Arctic sea ice. J. Geophys. Res. Oceans 120 (9), 5932—5944, http://dx.doi.org/10.1002/2015JC010914.

Kou, L., Labrie, D., Chylek, P., 1993. Refractive indices of water and ice in the 0.65- to 2.5-μm spectral range. Appl. Opt. 32 (19), 3531—3540, http://dx.doi.org/10.1364/AO.32.003531.

Lei, R., Tian-Kunze, X., Leppäranta, M., Wang, J., Kaleschke, L., Zhang, Z., 2016. Changes in summer sea ice, albedo, and portioning of surface solar radiation in the Pacific sector of Arctic Ocean during 1982—2009. J. Geophys. Res. Oceans 121 (8), 5470—5486, http://dx.doi.org/10.1002/2016JC011831.

Leppäranta, M., 2009. A two-phase model for thermodynamics of floating ice. In: Proceedings of the 6th Workshop on Baltic Sea Ice Climate, Report Series in Geophysics, 61. Dept. Physics, Univ. Helsinki, Finland, 146—154.

Leppäranta, M., 2015. Freezing of Lakes and the Evolution of their Ice Cover. Springer, Heidelberg, 301 pp., http://dx.doi.org/10.1007/978-3-642-29081-7.

Leppäranta, M., Reinart, A., Arst, H., Erm, A., Sipelgas, L., Hussainov, M., 2003. Investigation of ice and water properties and under-ice light fields in fresh and brackish water bodies. Nord. Hydrol. 34 (3), 245—266.

Light, B., Grenfell, T.C., Perovich, D.K., 2008. Transmission and absorption of solar radiation by Arctic sea ice during the melt season. J. Geophys. Res. 113 (C3), 19 pp., http://dx.doi.org/10.1029/2006JC003977.

Light, B., Maykut, G.A., Grenfell, T.C., 2003. Effects of temperature on the microstructure of first-year Arctic sea ice. J. Geophys. Res. 108 (C2), 16 pp., http://dx.doi.org/10.1029/2001JC000887.

Light, B., Perovich, D.K., Webster, M.A., Polashenski, C., Dadic, R., 2015. Optical properties of melting first-year Arctic sea ice. J. Geophys. Res. Oceans 120 (11), 7657—7675, http://dx.doi.org/10.1002/2015JC011163.

Lu, P., Leppäranta, M., Cheng, B., Li, Z., 2016. Influence of melt-pond depth and ice thickness on Arctic sea-ice albedo and light transmittance. Cold Reg. Sci. Technol. 124 (1), 1—10, http://dx.doi.org/10.1016/j.coldregions.2015.12.010.

Maykut, G.A., Untersteiner, N., 1971. Some results from a time dependent, thermodynamic model of sea ice. J. Geophys. Res. 76 (6), 1550—1575, http://dx.doi.org/10.1029/JC076i006p01550.

Morassutti, M.P., Ledrew, E.F., 1996. Albedo and depth of melt ponds on sea-ice. Int. J. Climatol. 16 (7), 817—838, http://dx.doi.org/10.1002/(SICI)1097-0088(199607)16:7<817::AID-JOC44>3.0.CO;2-5.

NASA/Goddard Space Flight Center, 2014. Satellites Measure Increase of Sun's Energy Absorbed in the Arctic. Science Daily, http://www.sciencedaily.com/releases/2014/12/141217154124.htm (retrieved 10.10.17).

Nicolaus, M., Katlein, C., Maslanik, J., Hendricks, S., 2012. Changes in Arctic sea ice result in increasing light transmittance and absorption. Geophys. Res. Lett. 39 (24), 6 pp., http://dx.doi.org/10.1029/2012GL053738.

Pedersen, C.A., Roeckner, E., Lüthje, M., Winthere, J.-G., 2009. A new sea ice albedo scheme including melt ponds for ECHAM5 general circulation model. J. Geophys. Res. 114 (D8), 15 pp., http://dx.doi.org/10.1029/2008JD010440.

Perovich, D.K., 1990. Theoretical estimates of light reflection and transmission by spatially complex and temporally varying sea ice covers. J. Geophys. Res. 95 (C6), 9557—9567, http://dx.doi.org/10.1029/JC095iC06p09557.

Perovich, D.K., 1996. The optical properties of sea-ice. Cold Reg. Res. and Eng. Lab. (CRREL) Report 96-1, Hanover, NH, 31 pp.

Perovich, D.K., 2005. On the aggregate-scale partitioning of solar radiation in Arctic sea ice during the Surface Heat Budget of the

Arctic Ocean (SHEBA) field experiment. J. Geophys. Res. 110 (C3), 12 pp., http://dx.doi.org/10.1029/2004JC002512.

Perovich, D., Richter-Menge, J., Tucker, W., 2001. Seasonal changes in Arctic sea-ice morphology. Ann. Glaciol. 33 (1), 171—176, http://dx.doi.org/10.3189/172756401781818716.

Perovich, D., Tucker, W., 1997. Arctic sea-ice conditions and the distribution of solar radiation during summer. Ann. Glaciol. 25 (1), 445—450, http://dx.doi.org/10.3189/S0260305500014439.

Podgorny, I., Grenfell, T.C., 1996. Partitioning of solar energy in melt ponds from measurements of pond albedo and depth. J. Geophys. Res. 101 (C10), 22737—22748, http://dx.doi.org/10.1029/96JC02123.

Podgorny, I., Lubin, D., Perovich, D.K., 2018. Monte Carlo study of UAV-measurable albedo over Arctic sea ice. J. Atmos. Oceanic Technol. 35 (1), 57—66, http://dx.doi.org/10.1175/JTECH-D-17-0066.1.

Polashenski, C., Perovich, D., Courville, Z., 2012. The mechanisms of sea ice melt pond formation and evolution. J. Geophys. Res. 117 (C1), 23 pp., http://dx.doi.org/10.1029/2011JC007231.

Polyakov, I.V., Pnyushkov, A.V., Alkire, M.B., Ashik, I.M., Baumann, T. M., Carmack, E.C., Goszczko, I., Guthrie, J., Ivanov, V.V., Kanzow, T., Krishfield, R., Kwok, R., Sundfjord, A., Morison, J., Rember, R., Yulin, A., 2017. Greater role for Atlantic inflows on sea-ice loss in the Eurasian Basin of the Arctic Ocean. Science 356 (6335), 285—291, http://dx.doi.org/10.1126/science.aai8204.

Reinart, A., Arst, H., Blanco-Sequeiros, A., Herlevi, A., 1998. Relation between underwater irradiance and quantum irradiance in dependence on water transparency at different depths in the water bodies. J. Geophys. Res. 103 (C4), 7749—7752, http://dx.doi.org/10.1029/97JC03645.

Shokr, M., Sinha, N., 2015. Sea Ice: Physics and Remote Sensing. John Wiley & Sons, Inc., Hoboken, NJ, 99—137, http://dx.doi.org/10.1002/9781119028000.

Skyllingstad, E.D., Paulson, C.A., Perovich, D.K., 2009. Simulation of melt pond evolution on level ice. J. Geophys. Res. 114 (C12), 15 pp., http://dx.doi.org/10.1029/2009JC005363.

Smith, R.C., Baker, K.S., 1981. Optical properties of the clearest natural waters (200—800 nm). Appl. Opt. 20 (2), 177—184, http://dx.doi.org/10.1364/AO.20.000177.

Taskjelle, T., Hudson, S.R., Granskog, M.A., Nicolaus, M., Lei, R., Gerland, S., Stamnes, J.J., Hamre, B., 2015. Spectral albedo and transmittance of thin young Arctic sea ice. J. Geophys. Res. Oceans 121 (1), 540—553, http://dx.doi.org/10.1002/2015JC011254.

Taylor, P.D., Feltham, D.L., 2004. A model of melt pond evolution on sea ice. J. Geophys. Res. 109 (C12), 19 pp., http://dx.doi.org/10.1029/2004JC002361.

Wang, C., Granskog, M.A., Gerland, S., Hudson, S.R., Perovich, D.K., Nicolaus, M., Karlsen, T.I., Fossan, K., Bratrein, M., 2014. Autonomous observations of solar energy partitioning in first-year sea ice in the Arctic Basin. J. Geophys. Res. Oceans 119 (3), 2066—2080, http://dx.doi.org/10.1002/2013JC009459.

Wang, C., Granskog, M.A., Hudson, S.R., Gerland, S., Pavlov, A.K., Perovich, D.K., Nicolaus, M., 2016. Atmospheric conditions in the central Arctic Ocean through the melt seasons of 2012 and 2013: Impact on surface conditions and solar energy deposition into the ice—ocean system. J. Geophys. Res. Atmos. 121 (3), 1043—1058, http://dx.doi.org/10.1002/2015JD023712.

Webster, M.A., Rigor, I.G., Perovich, D.K., Richter-Menge, J.A., Polashenski, C.M., Light, B., 2015. Seasonal evolution of melt ponds on Arctic sea ice. J. Geophys. Res. Oceans 120 (9), 5968—5982, http://dx.doi.org/10.1002/2015JC011030.

Zhang, S., Zhao, J., Shi, J., Jiao, Y., 2014. Surface heat budget and solar radiation allocation at a melt pond during summer in the central Arctic Ocean. J. Ocean Univ. China 13 (1), 45—50, http://dx.doi.org/10.1007/s11802-014-1922-0.